Characterization and performance of the upgraded NIRSPEC on the W. M. Keck Telescope

López, Ronald, Hoffman, Erika, Doppmann, Greg, Fitzgerald, Michael, Johnson, Chris, et al.

Ronald A. López, Erika B. Hoffman, Greg Doppmann, Michael P. Fitzgerald, Chris Johnson, Marc Kassis, Kyle Lanclos, Jim Lyke, Emily C. Martin, Ian McLean, Ji Man Sohn, Jason Weiss, "Characterization and performance of the upgraded NIRSPEC on the W. M. Keck Telescope," Proc. SPIE 11447, Ground-based and Airborne Instrumentation for Astronomy VIII, 114476B (28 December 2020); doi: 10.1117/12.2563075

Event: SPIE Astronomical Telescopes + Instrumentation, 2020, Online Only

Characterization and Performance of the Upgraded NIRSPEC on the W. M. Keck Telescope

Ronald A. López[a], Erika B. Hoffman[a], Greg Doppmann[b], Michael P. Fitzgerald[a], Chris Johnson[a], Marc Kassis[b], Kyle Lanclos[b], Jim Lyke[b], Emily C. Martin[c], Ian McLean[a], Ji Man Sohn[a], and Jason Weiss[a,d]

[a]Department of Physics & Astronomy, University of California, Los Angeles, 430 Portola Plaza, Box 951547, Los Angeles, CA 90095, USA
[b]W. M. Keck Observatory, 65-1120 Mamalahoa Highway, Kamuela, HI 96743, USA
[c]University of California, Santa Cruz, 1156 High Street Santa Cruz, CA 95064, USA
[d]TMT International Observatory, 100 West Walnut Street, Suite 300 Pasadena, CA 91124, USA

ABSTRACT

NIRSPEC is a high-resolution near-infrared echelle spectrograph on the Keck II telescope that was commissioned in 1999 and upgraded in 2018. This recent upgrade was aimed at improving the sensitivity and longevity of the instrument through the replacement of the spectrometer science detector (SPEC) and slit-viewing camera (SCAM). Commissioning began in 2018 December, producing the first on-sky images used in the characterization of the upgraded system. Through the use of photometry and spectroscopy of standard stars and internal calibration lamps, we assess the performance of the upgraded SPEC and SCAM detectors. First, we evaluate the gain, readnoise, dark current, and the charge persistence of the spec detector. We then characterize the newly upgraded spectrometer and the resulting improvements in sensitivity, including spectroscopic zero points, pixel scale, and resolving power across the spectrometer detector field. Finally, for SCAM, we present zero points, pixel scale, and provide a map of the geometric distortion of the camera.

Keywords: Infrared, Spectroscopy, Spectrograph, Detectors, High Resolution, Keck, Characterization, Upgrade

1. INTRODUCTION

NIRSPEC is a near-infrared echelle spectrograph on the W. M. Keck II telescope commissioned in 1999.[1,2] NIRSPEC's cryostat is equipped with two detectors: a slit viewing camera (SCAM) and a spectrometer detector (SPEC). The SPEC detector is sensitive to a wavelength range of 1-5 μm and capable of both low resolution (R$\sim$2000) and high-resolution (R$\sim$25,000) observations. As part of the 2018 NIRSPEC upgrade,[3] both the SCAM and SPEC detectors were replaced in order to improve the sensitivity and longevity of the instrument. The original Aladdin III InSb 1024$\times$1024 array used in SPEC was replaced by a Teledyne Hawaii-2RG (H2RG) HgCdTe 2048$\times$2048 array. The H2RG's larger detector size and smaller (18 μm) pixel size enables increased sensitivity and higher signal-to-noise measurements. The original PICNIC 256$\times$256 array in SCAM has also been replaced by an engineering-grade H2RG, increasing the sensitivity range of SCAM from 1–2.5 μm to 1–5 μm. The use of the full 2048$\times$2048 array of the SCAM H2RG is not needed as the field of view is small enough to use only a portion of the detector. Using a 256$\times$256 sub-array allows for faster readout speeds. Here we report the characteristics of the upgraded detectors, along with helpful information for the use of NIRSPEC on sky. In Section 2, we discuss the characterization of the SPEC detector and in Section 3, we discuss the characterization of the SCAM detector. In Section 4, we summarize the analysis done in this paper.

Further author information: (Send correspondence to Ronald A. Lopez)
Ronald A. Lopez: E-mail: rlopez@astro.ucla.edu

Ground-based and Airborne Instrumentation for Astronomy VIII, edited by Christopher J. Evans, Julia J. Bryant, Kentaro Motohara, Proc. of SPIE Vol. 11447, 114476B · © 2020 SPIE · CCC code: 0277-786X/20/$21 · doi: 10.1117/12.2563075

2. SPEC

The SPEC detector is the workhorse of NIRSPEC. SPEC is primarily used in taking high-resolution spectra in a large wavelength range (1–5 μm) and has produced many successful scientific results ranging from solar system science to extragalactic astronomy.[4] In Section 2.1 we report the gain of the SPEC detector. In Section 2.2 we discuss the instrument background. In Section 2.3 we discuss the readnoise and suspected contributions from the instrument background on the readnoise levels. In Sections 2.4 and 2.5 we report the flux zero points and throughput for the NIRSPEC filters N1, N3, N5, and N7. In Section 2.6 we briefly discuss the persistence of the detector. In Sections 2.7 and 2.8 we report the the pixel scale and spectral dispersion of SPEC. Lastly, in Section 2.9 we discuss and provide a map of the resolving power across the detector.

2.1 Gain

The first step we take in understanding the behavior of the SPEC detector is measuring the gain. Here we measure the conversion gain, the ratio of photoelectrons (e^-) per analog-to-digital unit (ADU). We use a series of flat-field exposures with increasing exposure times to measure the gain. First, a bad pixel map is created by taking the ratio between two flats of different exposure times and marking pixels with values 3-sigma outside the value expected for the ratio of normal pixels. The bad pixel map is applied to each image, removing hot and cold pixels from consideration. The calculation of the gain follows a simplified and modified version of the methods described in Mortara and Fowler (1981).[5] We first take the difference between the flats, however, during the process of taking flats, the lamp increases in temperature and flats taken later in the run tend to be brighter than those taken earlier. To compensate for this, we take the ratio between two flats with equal exposure times and use this as a scaling factor to normalize the first image to the same light level as the second. Once this correction is made, the flats should be scaled to the same light level and can be differenced. The gain itself is determined by the slope of the relationship between the mean and variance of the differenced frame. In Figure 1, we plot the means and variances of flat field pairs of increasing exposure time and overplot a linear fit to the data, yielding a gain of 3.01 ± 0.08 e^- /ADU

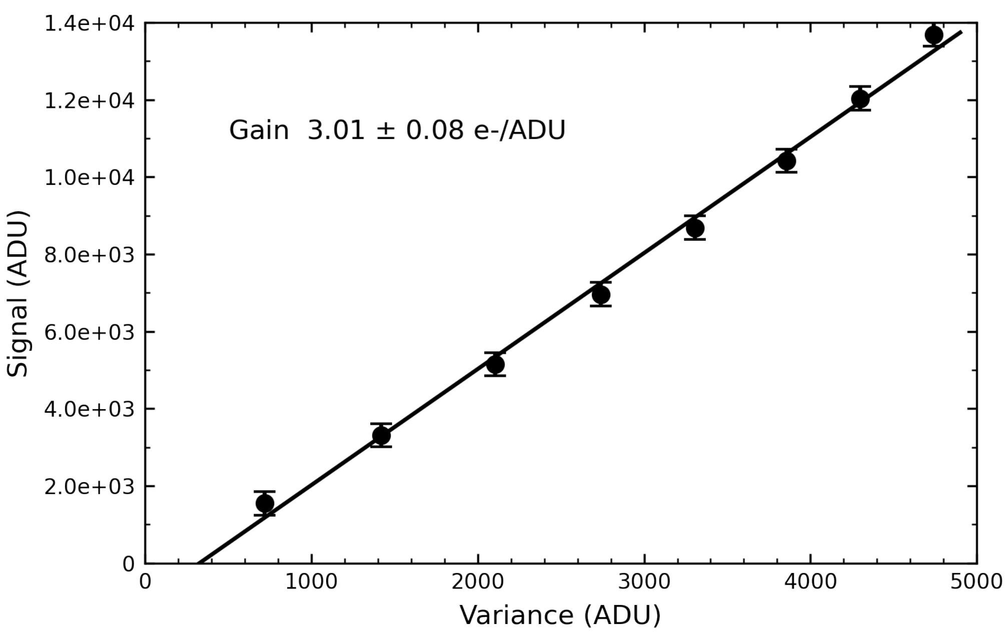

Figure 1. SPEC detector gain. The mean values of the processed flat images are plotted on the Y axis and the variance on the X axis. The gain is the slope of the best-fit line, which we measure to be 3.01 ± 0.08 e^-/ADU.

2.2 Instrument Background

In this section, we characterize the signal recorded when there are no expected photons interacting with the detector. In normal circumstances the background level of the detector is dominated by the dark current which builds over time. For this paper, we will simply refer to this as the "instrument background" ascribed to a potential light leak contributing to the background levels by thermal photons. We determine this background by measuring the signal of dark frames of increasing exposure times. The background is calculated by taking the mean of the dark frames after removing bad pixels. The signal is then plotted against integration time in Figure 2 and fit with a line to determine the rate of change of the instrument background and integration time. The slope of this line is then multiplied by the gain to yield an instrument background of 0.70 ± 0.10 e^- /s.

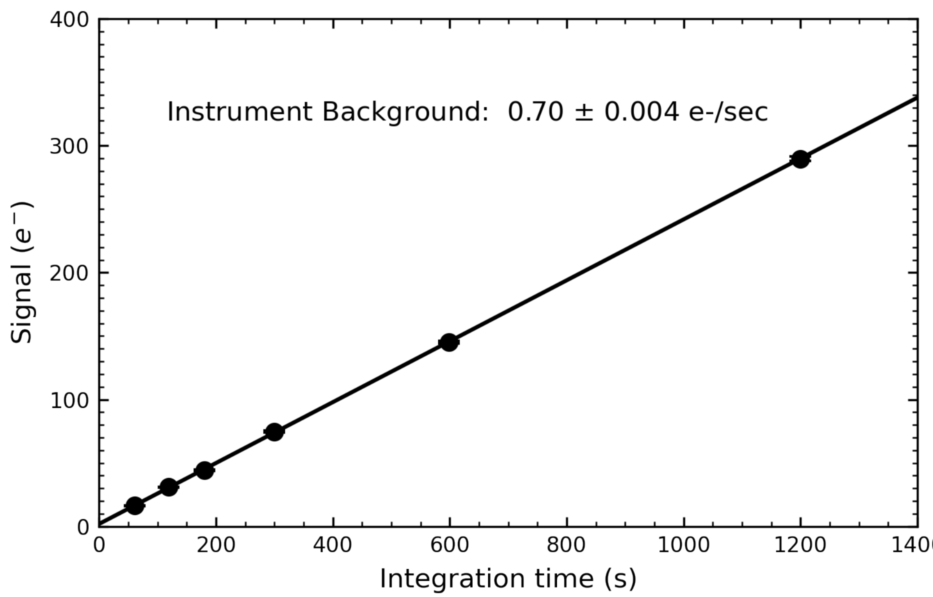

Figure 2. The instrument background is determined using the slope of the best fit line to the signal measurements. We measure an elevated background level of 0.70 ± 0.10 e^- /s which is consistent with a light leak and is at or below that from previous array.

A major motivation for the detector upgrade to the H2RG was the promise of a much reduced dark current than the Aladdin III. The H2RG array is manufactured to achieve dark currents of less than 0.05 e^-/s.[6] The elevated background signal we measure is consistent with a light leak. Figure 3 shows an example dark frame with an exposure time of 20 minutes. The long exposure time makes it easy to see contributions from a large external signal. In Figure 3, we plot a histogram of the background levels across the entire frame. For an instrument background dominated by dark current, we expect one peak in the background rate, however the histogram shows multiple peaks. This elevated background is also consistent with background levels of the previous Alladin III, measured to be between 0.7–1.0 e^- /s. This suggests that the light leak may have gone undetected in the old configuration. Attempts to identify and correct the source of the light leak are ongoing. So far, modulation of the slit, the echelle grating, and the cross-disperser do not appear to modulate the pattern, suggesting the leak is occurring in the backend camera.

2.3 Readnoise

We further characterize the SPEC detector by measuring the readnoise. Knowledge of the readnoise levels is important for short-exposure time performance of the spectrometer. To measure the readnoise, we take the difference between two dark frames of equal exposure time, compute the standard deviation, and divide by $\sqrt{2}$

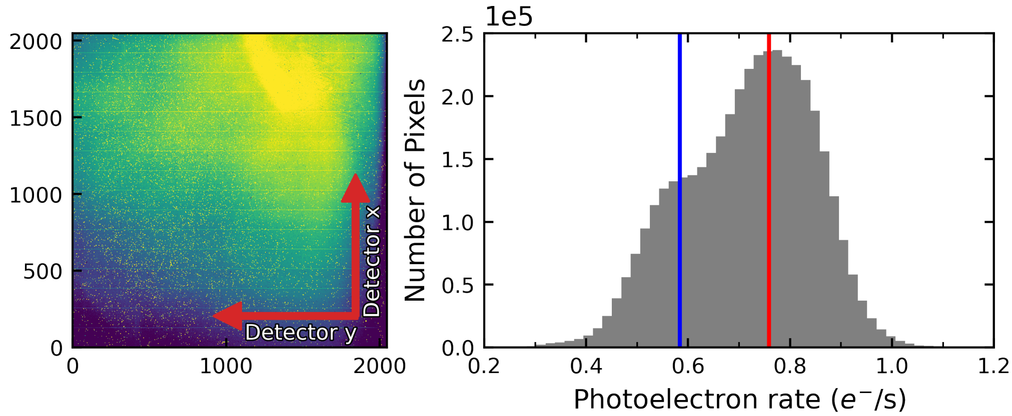

Figure 3. Left: sample 20-minute dark frame. With long exposure times, the elevated signal can be seen clearly in the upper right corner of the frame. Right: histogram of the photoelectron rate in e^{-}/s. The blue and red lines are the peaks of two distributions that contribute to the elevated instrument background.

to compensate for double counting. This gives us a measurement of the noise in a single frame. This is done for 5 pairs of dark frames, all of equal exposure times. The mean of these 5 measurements gives the final noise value and the variance of these values gives the uncertainty on the mean readnoise. The noise in ADU is multiplied by the gain to convert to electrons. This process is then repeated for dark exposures of increasing number of reads and exposure time. The increase in exposure time is needed to compensate for the 1.5 s clock time of reading out the detector. For this experiment, the array is read out using either correlated double sampling (CDS) or multiple correlated double sampling (MCDS) modes. Thus for each set, N refers to the number of Fowler pairs, or the number of reads taken at the beginning and end of each exposure. For example, CDS corresponds to $N = 1$ and MCDS 16 corresponds to $N = 16$.

Figure 4 provides the measured value of readnoise as a function of number of Fowler pairs. We expect that for uncorrelated noise which has the same value for all reads, the noise should decrease as $\sqrt{N}$. While we do see a decrease in readnoise, it goes as $N^{-0.42}$. The difference in the exponent is likely due in part to the elevated instrument background that we observe in Figure 3. The exposure time increases with the number of reads due to the time required to read out the detector. As a consequence, the exposures with more reads receive non-negligible shot noise contributions from the elevated instrument background. In an attempt to remove the bias caused by the background, we subtract out the variance of the background from the measured noise data, which for Poisson distributions is just the mean of the dark frames. In Figure 4, we plot both the measured readnoise as well as the bias subtracted noise. In an attempt to find the exact relation between readnoise and number of reads, we fit a power law to all of these data except the last point. We exclude the last point at 16 reads because we suspect that noise contributions from other sources begin to dominate, thus the $1/\sqrt{N}$ behavior begins to break down greatly. The contribution of the shot noise is negligible at a small number of reads, but becomes significant at around 8 reads. This effect is non-negligible for longer exposure times and is most likely a strongly contributing factor to a higher than normal readnoise. However, additional unseen contributions to these elevated noise levels may still exist.

2.4 Zero points

We further characterize the SPEC detector by determining the zero points for the following filters: NIRSPEC-1, NIRSPEC-3, NIRSPEC-5, and NIRSPEC-7, which roughly correspond to the Y, J, H, and K bands respectively. Flux zero points provide a reference point for the signal strength on the detector for an astronomical source of known magnitude. They are helpful in characterizing instruments with non-standard filter sets and are useful for observation planning and assessing the performance of new detectors. On 2020 December 3rd, we took two exposures of the spectroscopic standard star SA 96-83 in each of the filters listed above using the $0.720'' \times 12''$

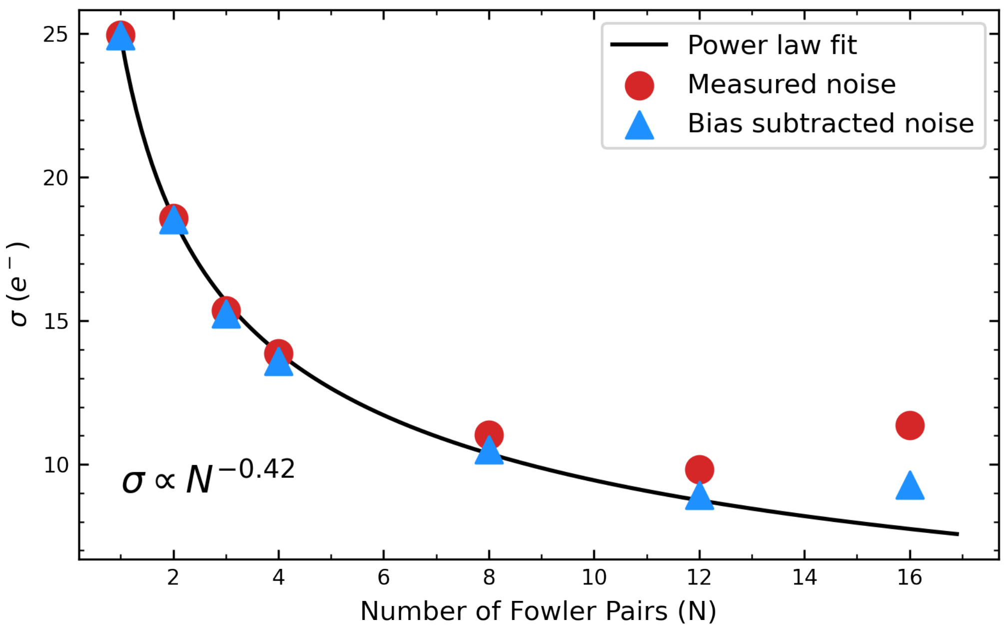

Figure 4. Readnoise as a function of number of reads (Fowler pairs). The red points are the measured noise values from the raw dark frames. The Blue triangles are the bias subtracted noise measurements calculated by subtracting the variance of the instrument background from the noise measurements. A power law is fit to all the bias subtracted noise data except for the 16 reads point. The readnoise decreases as a power law with power -0.42.

slit. We define the zero point as the monochromatic flux in Janskys corresponding to a signal of 1 ADU/s on the detector.

The SPEC zero points are determined by the total flux of the continuum of a standard star at a reference wavelength close to the band center. The reference wavelength is chosen by first identifying bright telluric emission lines in a high signal-to-noise region of the detector. These lines are used as a reference to determine the spectral dispersion locally, which allows for an accurate measure of the wavelength in a portion of the continuum between the telluric lines. Once a reference wavelength has been chosen, we take a 20-pixel-wide cut of the continuum in the spectral dimension centered at that wavelength and sum along the spatial dimension. Over this wavelength range, the continuum brightness is effectively constant, so this measurement of the mean brightness of the star accurately represents the star brightness at the reference wavelength. The uncertainty in this measurement is taken from the spread of each individual brightness measurement.

The average signal, divided by the integration time, provides a measure of flux in ADU/s. The known magnitude of the star is then converted to Janskys using the methods described in Tokunaga & Vacca (2005),[7] which contain conversion factors for the Mauna Kea Observatories near-IR filters. The conversion to monochromatic flux is defined at the isophotal wavelength, which is close but not equal to the reference wavelength used to determine the measured flux on the detector. We apply a small correction to the star flux by generating a blackbody curve using the spectral type of the star and calculating the ratio between the fluxes at the reference wavelength and the isophotal wavelength. The corrected star flux is then divided by the measured flux on the detector to determine the zero point flux in Janskys corresponding to 1 ADU/s. (See Table 1).

2.5 Throughput

Light can be extincted as it propagates through the atmosphere and through the instrument. Light is lost due to effects from the atmosphere, mirrors, filters, the slit, and several other potential sources. The total loss in transmission is the total throughput of the instrument. We aim to calculate the throughput in each of the

Table 1. SPEC Flux Zero Points.

Filter	Zero point (mJy)	Throughput (%)
NIRSPEC-1 (Y)	1.6 ± 0.3	17.0
NIRSPEC-3 (J)	1.80 ± 0.06	15.7
NIRSPEC-5 (H)	2.73 ± 0.11	9.7
NIRSPEC-7 (K)	1.09 ± 0.04	23.5

four NIRSPEC filters by comparing the expected photon rate from the star to the measured photon rate on the detector. We use the same data and methods described in Section 2.4 to derive a flux in Janskys and convert this value into a photon flux using the reference wavelength for the photon energy. The photon flux is then multiplied by the Keck telescope collecting area of 72 m^2, as reported by the observatory, and multiplied by the dispersion at the reference wavelength to account for a one-pixel-wide flux measurement on the detector. The measured flux in ADU/s/px is divided by the expected flux in ADU/s/px, providing the throughput. We list these values in Table 1. The measure of throughput is highly dependent on the seeing and slit loss, and these numbers can change depending on other observing conditions, but should be accurate at their order of magnitude level.

2.6 Persistence

Persistence refers to the charge that remains on the detector after a light source has been removed. Persistence can be an issue when taking an exposure after taking an image of a bright source. To characterize the persistence, we conduct an experiment using a group of saturated pixels. We took an exposure of a very saturated emission line then took a long exposure (1200 s) dark in quick succession and could not detect any residual signal within the noise ($\sigma = 13\ e^-$) of the same pixel region.

2.7 Pixel Scale

We calculate the pixel scale using the separation of known double stars aligned in the slit. Observations of the double star Struve 751 were taken in high-resolution mode using the N7 filter and $0.288'' \times 24''$ slit on 2020 December 3. Observations of UCAC 529-038252 were taken in low-resolution mode using the N1 filter and $42'' \times 0.380''$ slit on 2019 March 23. In both data sets, the thermal emission of the stars produces two traces on the detector along the wavelength dimension as shown in Figure 5. We calculate the plate scale by measuring the physical separation between the traces on the detector along the spatial dimension of the slit. The traces do not align with the orientation of the pixels due to their curvature. To account for this misalignment, the true separation was calculated by fitting a line to segments of each trace and a telluric line that bisects the two traces (Figure 5). The intersection of each trace with the telluric line produces a pair of coordinates which we use to calculate the pixel separation, and thus the physical distance between the traces. This measurement was calculated three times using different telluric lines and averaged to get the final measurement.

As outlined in Section 3.2, in low-resolution mode, we use an angular separation of $10.927 \pm 0.023''$ for the double star UCAC 529-038252, leading to a pixel scale of $0.098 \pm 0.004''$/px. For the high-resolution mode measurement, we use the angular separation of Struve 751 which is estimated using the most recent observations from Schlimmer (2015)[8] with an uncertainty based on the motion of the stars and the time since last observation. Using an angular separation of $15.54 \pm 0.20''$, we measure a pixel scale of $0.13 \pm 0.03''$/px.

2.8 Spectral Dispersion

The spectral dispersion is a measure of the change in wavelength on a per pixel basis, analogous to the pixel scale in wavelength space. The dispersion is dependent on the order and thus cannot be calculated using the same method as the pixel scale. Using IRAF packages `identify` and `dispcor`, we fit low order polynomials to arc lines of known wavelength. This gives a $\Delta\lambda$/px which is unique for each echelle order and uniform within each order.

In Figure 6, we plot the spectral dispersion as a function of order m and anchor a curve to the order $m = 60$. As expected for grating spectrometers, the spectral dispersion is inversely proportional to the order. Other than a few outliers, this curve matches very closely to the dispersion measurements.

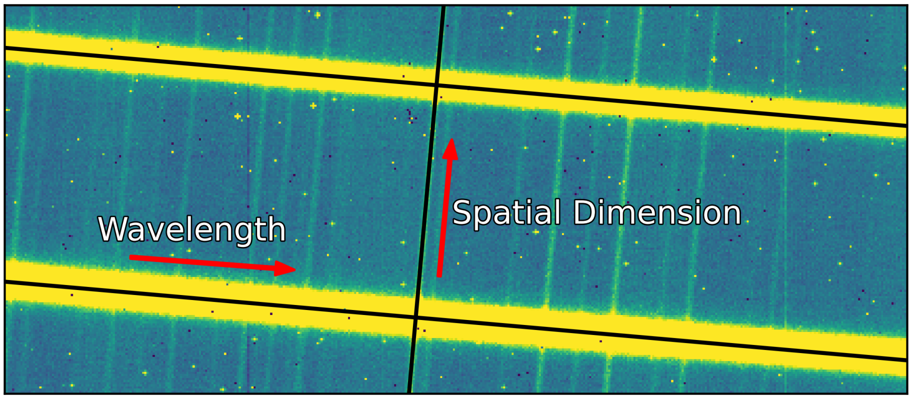

Figure 5. Double star image in low resolution mode depicting the two traces of the binary. The black lines are linear fits to the telluric line and stellar traces. The intersection of each pair of lines allows for accurate measures of the pixel separation of the two stars.

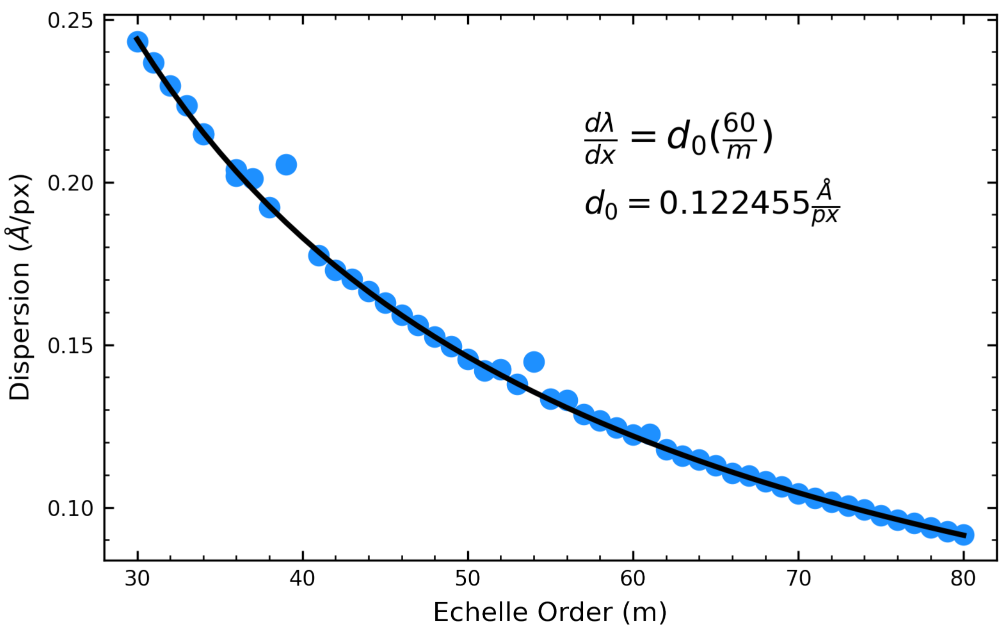

Figure 6. The spectral dispersion as a function of echelle order in the high-resolution mode on NIRSPEC. The curve is not a fit, but instead a curve anchored on the order $m = 60$. Other than a few outliers, the spectral dispersion is inversely proportional to echelle order m as expected for an echelle spectrograph.

2.9 Resolution Across the field

NIRSPEC was originally designed for a 1024×1024, 27-μm pixel Aladdin III, which set the optical prescription for the backend camera three-mirror anastigmat. The H2RG is physically larger, and can achieve greater spectral grasp, albeit at potentially reduced optical performance. Here we characterize the resolving power as a function of position in order to assess performance over the entire field of view and identify the highest resolution region of the detector. In order to determine the change in resolution across the detector, we measured the width of a large sample of calibration lines placed in varying positions on the detector. We used a series of 245 individual 1.5 s exposures taken with NIRSPEC's N5 filter and the $0.288'' \times 12''$ slit. Each frame contains an average of

~50 spectral lines from 4 calibration lamps (Argon, Krypton, Xenon, Neon) for a total of 11,750 data points. By stepping the spectra across the detector between each exposure, we ensured robust coverage of the entire frame. Each set of calibration lines are shifted in each exposure by altering the echelle and cross-disperser angles by 0.2° in order to obtain adequate coverage of the entire field. The exposures span a range of 62.0°–64.0° in echelle angle and 34.0°–38.0° in cross-disperser angle.

2.9.1 Measuring Line Width

The first step we take in determining the resolution across the field is creating a line finding algorithm that can reject unusable data like lines cut off by the edge of the detector. This algorithm takes in a NIRSPEC image, locates the positions of spectral lines and determines if the selected lines should be used in the analysis. The algorithm rejects lines that are either saturated or too dim, and rejects doublets or lines that are too close to each other. Each spectral line on the frame is uniquely angled relative to the orientation of the rows and columns of pixels on the detector due in part to the quasi-Littrow spectrometer configuration. For this reason, we do a line fit to each spectral line to find the angle of rotation locally and then de-rotate it. The width of a line is the FWHM of a Gaussian profile fitted to a row of pixels perpendicular to the emission line. This process is done for each row of pixels perpendicular to the line, creating a set of 40 width measurements per line. The median width value is used as the final width measurement of the line. This process is done for every identified line in the frame and is repeated for every exposure. The result is a large set of width measurements and their associated positions in the field.

2.9.2 Resolution Map

To create the map, we use the scikit-learn Birch clustering algorithm[9] to group the line width measurements based on their position on the detector. Each group contains a set of width measurements in a cell that are averaged to determine the resolution of the detector in their region. The position of the cell is determined by the geometric mean of each point in the group. A Voronoi diagram is then generated using these cells as seeds. The Voronoi diagram represents the mean resolution in each cell designated by a single color. The result is a color map illustrating the resolution across the detector as seen in Figure 7. The Voronoi diagram resembles a "plus" pattern with the lowest resolution in the corners and the highest resolution in the middle of the pattern. This pattern is consistent with the predictions of Martin et al. (2014)[10] which demonstrate, via ray tracing, a larger RMS spot size on the edges of the detector, with the largest spots in the corners. This result is not surprising as the optical performance is expected to be worse in these regions. Taking this into consideration, an observer can prioritize specific wavelengths in the highest resolution region of the detector by manipulating the echelle and cross-disperser angles.

3. SCAM

SCAM is used for target acquisition and guiding, providing a 40″ field of view surrounding each selected slit of the spectrograph. In Section 3.1 we report the magnitude zero points in the NIRSPEC filters N1, N3, N5, and N7. In Section 3.2 we report the pixel scale. In Section 3.3 we discuss in length our methods and results for the SCAM geometric distortion.

3.1 Zero points

To determine the zero points for SCAM, images of the UKIRT Faint Standard star FS 20 (G163-50; α = 11 07 59.93, δ = -05 09 26.1) were taken on 2019 March 23. Exposures at the minimum time were taken across the SCAM field in a square dither pattern with the star positioned off the slit. Four to nine exposures, 0.655 s each, were obtained in filters N1, N3, and N5, both with and without the short bandpass. For N7, images of the UKIRT Faint Standard star FS 10 (GD 50; α = 3 48 50.2, δ = -00 58 32) were taken 2020 December 3. Six exposures, 9.83 s each, were obtained in filter the N7 with only the short bandpass (called 'short' in Table 2). Filters N1, N3, N5, N7 correspond approximately to Y, J, H, and K bandpasses, respectively. The FS 20 images were reduced using standard techniques, specifically dark and sky subtraction, flat-fielding, and bad-pixel masking. Due to the small amount of data for each filter and the occasional bad pixels directly on the star, we attempt to reduce noise in our data by replacing the masked pixels by the median of the 4-pixel radius

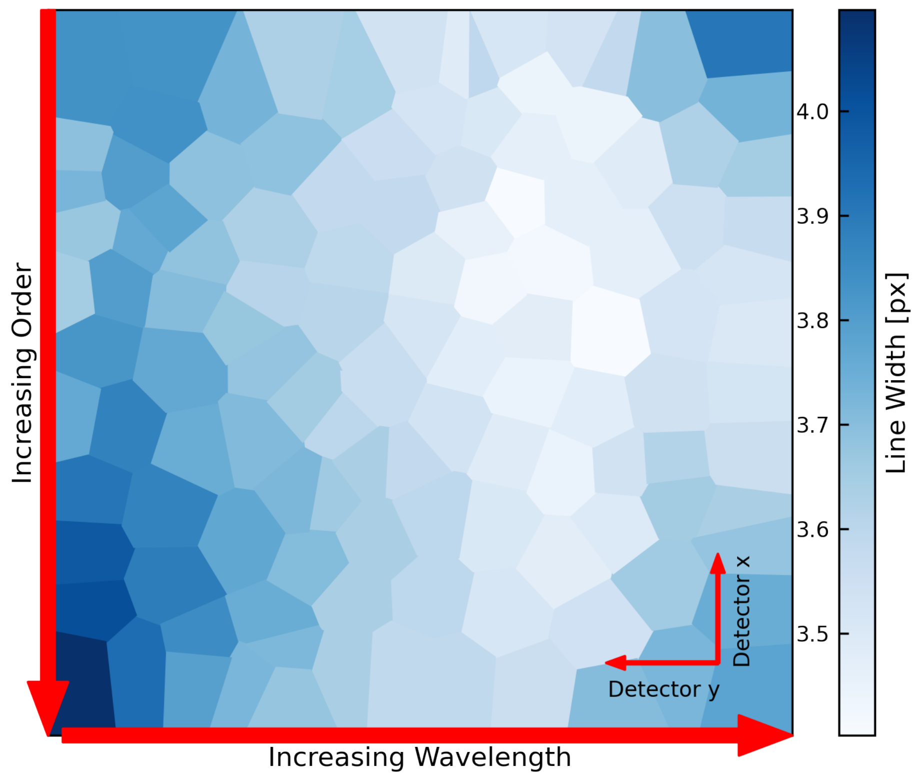

Figure 7. Voronoi diagram mapping the relative resolution of spectral lines. The resolution ranges from 3.4 to 4.1 pixels using the $0.288'' \times 12''$ slit in the N5 band. Lighter colors denote thinner lines and thus higher resolution. The resolution element of each individual region is determined using the mean resolution of lines enclosed by that region. The corners of the frame have the lowest resolution while the center of the "plus" pattern has the highest resolution.

circle around it. Each the star radius is comparatively 14 pixels. The zero points for each image are calculated individually and then converted to magnitudes corresponding to 1 ADU/s. The average for each filter was taken as the final result.

The SCAM zero point in N3 was found to be about 26.1 magnitudes, while the magnitude reported in McLean et al. (2000)[2] was 24.7. The improved sensitivity may be due to increased quantum efficiency of the new detector.

Table 2. SCAM Magnitude Zero Points.

Filter	Zero point Magnitude	Uncertainty
NIRSPEC 1	26.30	0.03
NIRSPEC 1 + short	26.26	0.01
NIRSPEC 3	26.11	0.02
NIRSPEC 3 + short	26.08	0.01
NIRSPEC 5	26.28	0.02
NIRSPEC 5 + short	26.22	0.02
NIRSPEC 7 + short	24.4	0.1

3.2 Pixel Scale

To determine SCAM's pixel scale, 30 images of the optical double star UCAC 529-038252 were taken with the target off the slit on 2019 March 23 (WDS 07106+1543; α = 07 10 37.92, δ =+15 43 14.2). Using the separation and proper motion measurements from Dugan et al. (2019)[11] we calculated the arcsecond separation by inserting the date for our night of observations into their equations of motion. We determined that the separation on our night was $10.86 \pm .023''$ which we divided by the averaged pixel separation to determine the scale. With an average separation of 69.1 ± 0.3 pixels, the pixel scale of SCAM was found to be $0.157 \pm 0.001''$/px.

3.3 Distortion

Optical distortion describes the changes in image magnification across the field of view, a consequence of the optical system. This effect means that the pixel scale can change across the detector, increasing error involved with acquisition and guiding. Mapping the distortion can reduce this error and allow for more accurate and reliable slit placement.

The 10 SCAM images of the Palomar 2 globular cluster used in this characterization were taken on 2019 March 21, with an exposure time of 5 s in the filter N1. Our methods follow the concept of 'self-calibration' and involve no external data.[12] The data contains exposures of Palomar 2, each taken on overlapping fields of view but shifted by at least a few arcseconds across.

Determining the distortion across the detector involved four major steps. We first catalogued the stars in their individual frames, which are within the detector exposure reference frame (Section 3.3.1). Second, we optimized their average positions in a larger master frame, which are in the reference frame of actual positions (Section 3.3.2). Third, we applied up to 4th-order polynomials to the transformation from the observed frames to the master frames (Section 3.3.3). The polynomial coefficients describe the best fit of the distortion across a single frame. Lastly, we conducted an array of tests to improve confidence in the solution (Section 3.3.4).

3.3.1 Identifying and Cataloguing Stars

The images were reduced using standard techniques, specifically dark and sky subtraction, flat-fielding, and bad-pixel masking. After basic data reduction, we designed a script that identifies stars through three major steps. In the first step, the script smooths each image with `scipy.ndimage.gaussian_filter` with a standard deviation of two. This reduces the strength of any leftover hot pixels. Second, the program applies `photutils.detection.find_peaks` to identify stars. In case the second step identifies still-persistent hot pixels instead of stars, a normalized inertia sifter, with a 10-pixel radius, checks to see if the surrounding area around the peak is also relatively bright, and if not, removes the data point from the list. Additionally, we check by visual inspection that all stars were correctly identified. The 10th frame yields significantly fewer stars then the rest, so is left out to ensure proper convergence for the overall fit.

Following the star identification, we organize each star by which exposure they are in and when they are repeat in another exposure. To do this, we not only run the star finding code on each individual exposure to find around 300 data points in total, but also the "Master Mosaic," shown in Figure 8, which come up with around 100 unique stars. The mosaic is constructed by arranging the exposures in the approximate positions relative to each other in the global reference frame, and averaging the exposure values of the portions that overlap. The averaging retrieves a similar background brightness throughout, which allows us to run the star-finding script again, and this time determining the approximate positions of the stars in the global reference frame.

Next, another script compares and matches stars in the global star list and individual frame list that are the same. To do so, the script transforms the star's x and y positions from the detector reference frame into the global reference frame, via approximate position used to place the exposure in the Master Mosaic. Since the exposure positions are still approximate at this stage, we check with a script that matching stars meet certain criteria. To determine which exposure data points correspond to a unique star, they must be both the closest stars in their individual and the global frame, and at most a radius of 5 pixels from each other. Some stars yield no match (likely meaning they were identified in the individual frame but not the global, or vice versa), but the unique stars that had at least two corresponding data, or in other words appeared in more than one exposure, went onto the next round of analysis. Note in Figure 8 how none of the yellow circled global reference frame stars are near the edges of the mosaic, because that would mean they had only one corresponding exposure data point. Similarly to how two values are needed to make a meaningful average, two data points to a single real star are needed to determine distortion.

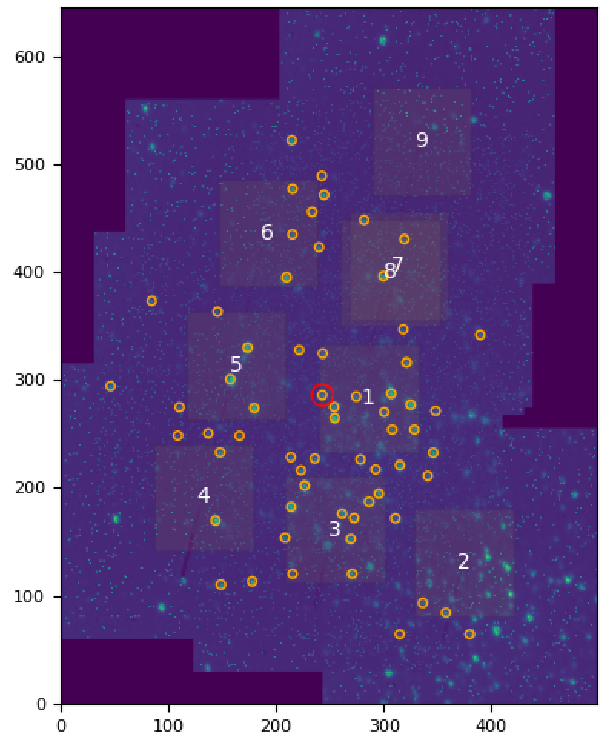

Figure 8. The Master Mosaic is the estimated initial guess for 63 on-sky stars in the globular cluster Palomar 2 and 9 frame relationships. The red circle identifies the "origin" star, which has a fixed position to avoid Mosaic shifting. Each of the 63 stars has 2 or more corresponding data points for which `scipy.optimize.leastsq` uses to optimize the Master Mosaic. The light-yellow squares are centered at each individual frame, and about one-eighth the size so each frame's approximate placement is visually discernible.

These global reference frame positions are approximate at this stage because we have not yet run any optimization or corrected for any distortion yet, but they are sufficient to cross-reference with the data in the individual frames, and later use as an initial guess for the optimization because they are unique on-sky stars. The ∼300 data points for the individual frames are by contrast 'exact' in the sense that they are the data of the distortion in the reference frame of the detector. If this were a linear optimization problem, the individual exposure data would be the scatter of the scatter plot, and the unique global star positions would be the line we are trying to best-fit.

3.3.2 Distortion-less Solution

The fitting function uses each approximate unique star position and exposure placements in the global reference frame as the initial guess for the unique star's parameters and exposure position parameters. Using `scipy.optimize.leastsq`, the fitter optimized the placement of these global parameters in comparison to the data in the individual frames. One star was left out of the parameters, which could be thought of as the 'anchor,' to avoid degeneracy in the shifting of the entire global reference frame (red circle in Figure 8). The anchor star was positioned at the center to minimize parameter correlations, although moving the origin does not actually change the best fit. The optimized model at this point of the process could be considered as the "distortion-less" solution, because the solution represents the averaged locations of the Palomar 2 stars taken from images.

3.3.3 Applying Distortion

After determining the best average global star and exposure positions, the model applies a polynomial transformation from the distorted star positions in their individual exposures. The best-fit polynomial transformation is the distortion solution. We used 1st-, 2nd-, 3rd-, and then 4th-order polynomials for accumulating a better guess and finding the most exact solution. A new polynomial parameter is only kept if the solution retains a lower reduced chi squared while determining the best fit of the distortion across the detector. Note equations 1 and 2 show the 4th order polynomial transformations.

$$X_{\text{global}}(x, y) = \cancel{a_0} + X_0 + \cancel{a_1 x} + \cancel{a_2 y} + a_3 xy + a_4 x^2 + a_5 y^2 + a_6 x^2 y + a_7 xy^2 + a_8 x^3 + a_9 y^3 \tag{1}$$

$$Y_{\text{global}}(x, y) = \cancel{b_0} + Y_0 + \cancel{b_1 x} + \cancel{b_2 y} + b_3 xy + b_4 x^2 + b_5 y^2 + b_6 x^2 y + b_7 xy^2 + b_8 x^3 + b_9 y^3 \tag{2}$$

a and b are new parameters the fitter must also optimize, and x and y are the star positions from the individual frames. a_0 and b_0 are removed to avoid degeneracy with the star position parameters. Also, we define the origin of the distortion at the center according to Equation 3 because the detector is a square 256×256 pixel array.

$$X_0 = Y_0 = 256/2 = 128 \tag{3}$$

We suspected degeneracy with the linear terms as well and confirmed it through principle component analysis of the fit covariance. After a_1, a_2, b_1 and b_2 are then removed as free parameters to avoid anamorphic distortion degeneracy with the scaling of both frames and stars. Since the star positions are kept as parameters during the polynomial fitting, the linear polynomials are redundant through the possibility of image magnification.

The final analysis is completed with 63-star parameters in the global reference frame, and 200 data points across 9 exposures, as shown in Figure 9. To ensure that we find the solution with the lowest χ^2, we test the convergence with different combinations of parameters. The best solution does not use every polynomial parameter. The final polynomial solution, transitioning from the distorted frame to the undistorted frame, is described in Tables 4 and 5.

Table 3. SCAM Polynomial Distortion Coefficients.

$(X)_{\text{global}}$	1	x	x^2	x^3
1	X_0	a_1	a_4	a_8
y	a_2	a_3	a_6	0
y^2	a_5	a_7	0	0
y^3	a_9	0	0	0

Table 4. SCAM Polynomial Distortion Coefficients.

X_{global}	1	x	x^2	x^3
1	128	1	0	1.6e-7 ± 4e-7
y	0	0	5.5e-7 ± 3e-7	0
y^2	6e-5 ± 2e-5	0	0	0
y^3	5.9e-7 ± 2e-7	0	0	0

Table 5. SCAM Polynomial Distortion Coefficients.

Y_{global}	1	x	x^2	x^3
1	128	0	-1.5e-5 ± 2e-5	1.5e-7± 4e-7
y	1	9.3e-6 ± 2e-5	-6.7e-7 ± 3e-7	0
y^2	-5.8e-5 ± 2e-5	-8.4e-7 ± 3e-7	0	0
y^3	0	0	0	0

Figure 9 shows the exaggerated final solution and with corresponding uncertainty. The small red points represent the Gaussian uncertainty distribution for each transformation vector on the figure. The red dots are calculated by using polynomial coefficient covariance after being converted into detector position with 100 random 2-D Gaussian samples. Uncertainty increases at the edges due to both increased distortion and scarcity of data.

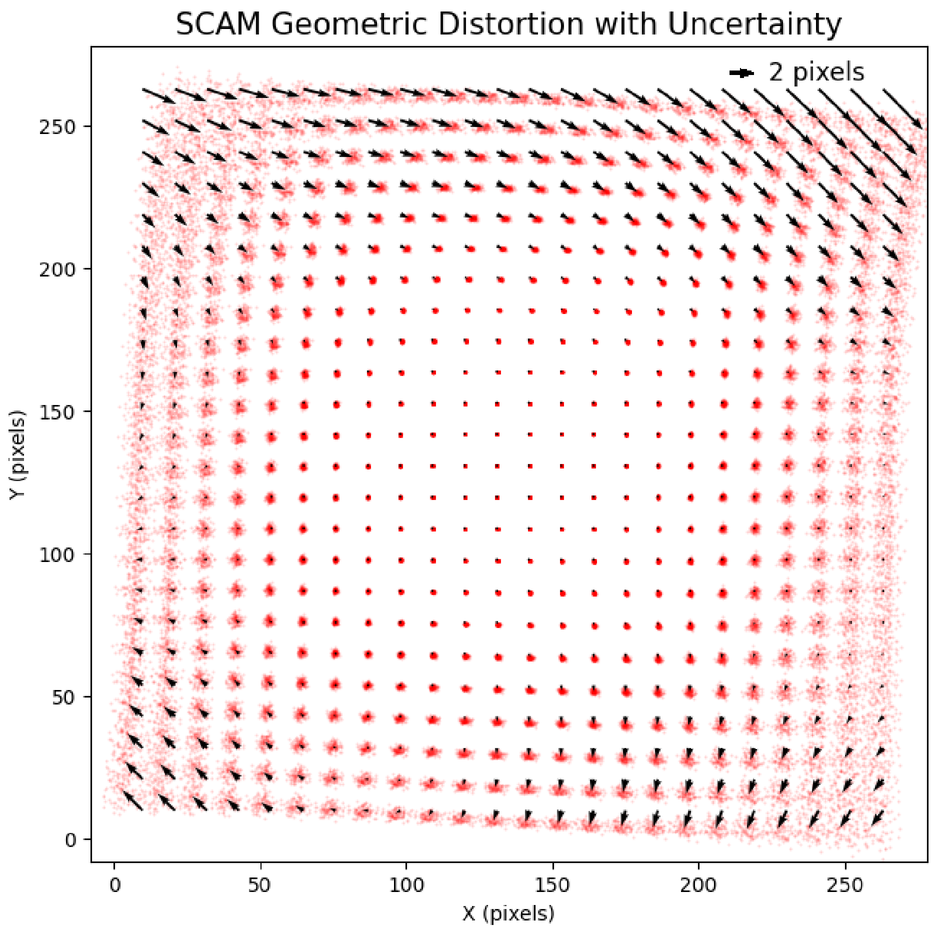

Figure 9. The exaggerated geometric distortion vector plot solution across the SCAM detector. The arrows point in the direction of translation, from observed (distorted) positions to real (undistorted) positions. The clouds of red dots represent the positional uncertainty of the undistorted position.

3.3.4 Ensuring Fit Confidence

Upon inspecting the correlation matrices of all optimized parameters to search for other possible degeneracies, it seems at first that the correlations between star and frame parameters were relatively high. Through further inspection and tests, the correlations were highly dependent on the origin star, and how many frames the origin star appeared in the real data. We chose an origin star which overlapped with the maximum number of overlapping frames, but it could not be all due to the large spread of data across the detector. Regardless, the choice of origin star had no effect on the converged solution in any tests of real or synthetic data.

To ensure confidence in the fitter, we tested for recovery of synthetic data, both with and without synthetic uncertainty. The first tests contained no synthetic uncertainty, and confirmed basic success in fitter's ability to find the solution, even with an in-exact guess. The next synthetic data tests included uncertainty using `Numpy.Random.RandNumber` generator. The error bars of the optimized solution to synthetic data were within at least two third of the correct solution. This gives us confidence that with Gaussian uncertainty, our model and fitter can find a meaningful distortion solution.

4. SUMMARY

We presented on the characterization on two of the NIRSPEC detectors, SPEC and SCAM. We begin with a report of the gain on the SPEC detector. Darks from the SPEC detector show an elevated instrument background of 0.70 ± 0.10 e^- /s caused by a light leak in the backend camera. The elevated background levels on SPEC appear to contribute to increases in readnoise at long exposure times. We report the flux zero points and throughputs in four NIRSPEC filters: N1, N3, N5, and N7. The persistence on the SPEC detector is undetectable down to the noise. We measure a pixel scale of $0.098 \pm 0.004''$/px in high-resolution mode and $0.1309 \pm 0.0750''$/px in low-resolution mode. The spectral dispersion across 50 orders follows a $1/m$ relation predicted from the grating equation. The resolution map of the SPEC detector verifies previous models predicting a decrease in performance in the corners of the detector and guides observers to the high-resolution region of the detector.

For SCAM we reported the magnitude zero points for the four NIRSPEC filters and for the first three filters with their short bandpass filters. The SCAM detector pixel scale is measured to be $0.157 \pm 0.001''$/px. Lastly, we presented on the geometric distortion of the SCAM detector and provide a distortion solution which can be used to correct for optical aberrations.

The next step in the characterization of the SPEC detector is to identify and remove the source of the light leak in the backend camera. Reducing the effects of this light leak will decrease the instrument background and improve the performance of SPEC at long exposure times. More data is currently being taken to identify more spectral lines out to longer wavelengths. These measurements will allows us to determine the spectral dispersion of the SPEC detector out to longer wavelengths and calculate the flux zero points for additional filters: KL, K-prime, L-prime, M-prime, M-wide, and possibly narrow-band filters H2, HeI, and FeII. For SCAM we are currently designing tests to determine the conversion gain, and in turn, the dark current, readnoise, and persistence. We also plan to extend the table of magnitude zero points to include the bands mentioned before as well as the throughput in each filter.

ACKNOWLEDGMENTS

We also thank W.M. Keck Observatory, which is operated as a scientific partnership among the California Institute of Technology, the University of California and the National Aeronautics and Space Administration. The Observatory was made possible by the generous financial support of the W.M. Keck Foundation. The authors wish to recognize and acknowledge the very significant cultural role and reverence that the summit of Maunakea has always had within the indigenous Hawaiian community. We are most fortunate to have the opportunity to conduct observations from this mountain. We would like to thank Michael Thacher for his generous contributions to help enable this work. We would also like to thank the Heising-Simons Foundation for their generous support of this project. This work was made possible in part by the National Science Foundation award AST-1532315. ECM acknowledges support from NSF Astronomy and Astrophysics Postdoctoral Fellowship under award AST-1801978.

REFERENCES

[1] McLean, I. S., Becklin, E. E., Bendiksen, O., Brims, G., Canfield, J., Figer, D. F., Graham, J. R., Hare, J., Lacayanga, F., Larkin, J. E., Larson, S. B., Levenson, N. G., Magnone, N., Teplitz, H. I., and Wong, W., "Design and development of NIRSPEC: a near-infrared echelle spectrograph for the Keck II telescope," in [*Infrared Astronomical Instrumentation*], Fowler, A. M., ed., **3354**, 566 – 578, International Society for Optics and Photonics, SPIE (1998).

[2] McLean, I. S., Graham, J. R., Becklin, E. E., Figer, D. F., Larkin, J. E., Levenson, N. A., and Teplitz, H. I., "Performance and results with the NIRSPEC echelle spectrograph on the Keck II telescope," in [*Optical and IR Telescope Instrumentation and Detectors*], Iye, M. and Moorwood, A. F. M., eds., **4008**, 1048 – 1055, International Society for Optics and Photonics, SPIE (2000).

[3] Martin, E. C., Fitzgerald, M. P., McLean, I. S., Doppmann, G., Kassis, M., Aliado, T., Canfield, J., Johnson, C., Kress, E., Lanclos, K., Magnone, K., Sohn, J. M., Wang, E., and Weiss, J., "An overview of the NIRSPEC upgrade for the Keck II telescope," in [*Ground-based and Airborne Instrumentation for Astronomy VII*], Evans, C. J., Simard, L., and Takami, H., eds., **10702**, 63 – 74, International Society for Optics and Photonics, SPIE (2018).

[4] McLean, I. S., "Science highlights from 4 years of nirspec on the keck ii telescope," in [*High Resolution Infrared Spectroscopy in Astronomy*], Käufl, H. U., Siebenmorgen, R., and Moorwood, A. F. M., eds., 25–36, Springer Berlin Heidelberg, Berlin, Heidelberg (2005).

[5] Mortara, L. and Fowler, A., "Evaluations of Charge-Coupled Device / CCD / Performance for Astronomical Use," in [*Society of Photo-Optical Instrumentation Engineers (SPIE) Conference Series*], *Society of Photo-Optical Instrumentation Engineers (SPIE) Conference Series* **290**, 28 (Jan. 1981).

[6] Blank, R., Anglin, S., Beletic, J. W., Bhargava, S., Bradley, R., Cabelli, C. A., Chen, J., Cooper, D., Demers, R., Eads, M., Farris, M., Lavelle, W., Luppino, G., Moore, E., Piquette, E., Ricardo, R., Xu, M., and Zandian, M., "H2RG focal plane array and camera performance update," in [*High Energy, Optical, and Infrared Detectors for Astronomy V*], Holland, A. D. and Beletic, J. W., eds., **8453**, 280 – 295, International Society for Optics and Photonics, SPIE (2012).

[7] Tokunaga, A. T. and Vacca, W. D., "The Mauna Kea Observatories Near-Infrared Filter Set. III. Isophotal Wavelengths and Absolute Calibration," *The Publications of the Astronomical Society of the Pacific* **117**, 421–426 (Apr. 2005).

[8] Schlimmer, J., "Double Star Measurements Using a Webcam and DSLR, Annual Report of 2014," *Journal of Double Star Observations* **11**, 149–153 (July 2015).

[9] Pedregosa, F., Varoquaux, G., Gramfort, A., Michel, V., Thirion, B., Grisel, O., Blondel, M., Prettenhofer, P., Weiss, R., Dubourg, V., Vanderplas, J., Passos, A., Cournapeau, D., Brucher, M., Perrot, M., and Duchesnay, E., "Scikit-learn: Machine learning in Python," *Journal of Machine Learning Research* **12**, 2825–2830 (2011).

[10] Martin, E. C., Fitzgerald, M. P., McLean, I. S., Adkins, S. M., Aliado, T., Brims, G., Johnson, C., Magnone, K., Wang, E., and Weiss, J., "Performance modeling of an upgraded NIRSPEC on Keck," in [*Ground-based and Airborne Instrumentation for Astronomy V*], Ramsay, S. K., McLean, I. S., and Takami, H., eds., **9147**, 2559 – 2565, International Society for Optics and Photonics, SPIE (2014).

[11] Dugan, O., Robinson, T., Carmeci, F., and Tock, K., "CCD Measurements and Reclassification of WDS 07106 +1543 to an Optical Double," *Journal of Double Star Observations* **15**, 119–129 (Jan. 2019).

[12] Libralato, M., Bellini, A., Bedin, L. R., Piotto, G., Platais, I., Kissler-Patig, M., and Milone, A. P., "Ground-based astrometry with wide field imagers - v. application to near-infrared detectors: Hawk-i@vlt/eso," *A&A* **563**, A80 (2014).